# *In situ* rheo-x-ray investigation of flow-induced orientation in layered silicate–syndiotactic polypropylene nanocomposite melt

Ashish Lele[a)]

*Department of Chemical Engineering, University of Cambridge, Cambridge CB2 3RA, United Kingdom and Chemical Engineering and Polymer Chemistry Division, National Chemical Laboratory, Pune 411 008, India*

Malcolm Mackley

*Department of Chemical Engineering, University of Cambridge, Cambridge CB2 3RA, United Kingdom*

Girish Galgali and C. Ramesh

*Chemical Engineering and Polymer Chemistry Division, National Chemical Laboratory, Pune 411 008, India*

(Received 19 October 2001; final revision received 3 June 2002)

**Synopsis**

This article describes experimental results for both the rheology and flow-induced orientation of a series of intercalated syndiotactic polypropylene nanocomposites which were prepared by melt intercalation in the presence or absence of an i-PP/maleic anhydride copolymer. The nanocomposites showed typical rheological signatures of well-dispersed interacalated nanocomposites such as a low frequency plateau in dynamic moduli and an apparent yield transition from very high viscosity at low shear stresses to low viscosity above a yield stress. *In situ* x-ray diffraction (XRD) measurements during shear provided direct evidence of rheology-microstructure links in these materials. It was found that the clay tactoids could be easily oriented by shear and that a high degree of orientation can be achieved after the yield transition. Further, the rheo-XRD apparatus allowed measurements of the relaxation of orientation upon the cessation of flow. The orientation relaxation time matched the characteristic relaxation times estimated from independent rheological measurements well. © *2002 The Society of Rheology.* [DOI: 10.1122/1.1498284]

## I. INTRODUCTION

Recent interest in polymer layered silicate (PLS) nanocomposites stems from the significant enhancement in thermomechanical and barrier properties of the materials achievable for clay loadings of as low as 5 wt %. These greatly improved properties depend on the dispersion and orientation of the highly anisotropic clay tactoids in the polymer matrix [see, for example, Kim *et al.* (2001); Brunside and Giannelis (1995); Messersmith and Giannelis (1994); Kojima *et al.* (1993)]. This paper is concerned with

[a)]Author to whom correspondence should be addressed; permanent address: Chemical Engineering Division, National Chemical Laboratory, Pune 411 008, India; electronic mail: lele@che.ncl.res.in

© 2002 by The Society of Rheology, Inc.

linking rheological measurements to an *in situ* investigation of the flow-induced microstructural evolution in these complex fluids.

Initial rheological studies on intercalated poly(dimethyl-co-diphenylsiloxane) nanocomposites [Krishnamoorti *et al.* 1996)] and end-tethered poly($\epsilon$-caprolactone) and nylon-6 nanocomposites [Krishnamoorti and Giannelis (1997)] have shown that the melts possess unusual viscoelastic properties such as nonterminal dynamic moduli at low frequency and a high shear thinning tendency. Further studies by Ren *et al.* (2000) on model monodisperse polystyrene-polyisoprene diblock copolymers showed that the rheology of PLS nanocomposites was not affected by the chemical nature of the polymer but rather by the mesoscopic structure of the hybrid. Small amplitude dynamic measurements indicated a solid-like response for time scales of the order of $10^3$ s and it was shown that the confinement of polymer chains within the galleries of the nanoclays did not contribute significantly to the rheological properties of the composite [Ren *et al.* (2000)]. It was suggested that for clay loadings in excess of 6.7 wt. % the clay tactoids form a percolating network as a result of physical jamming, which then offers considerable resistance to deformation and hence the solid-like behavior. Large amplitude dynamic data showed a decrease in the storage modulus and it was postulated that flow-induced alignment of the clay occurs at higher strain [Krishnamoorti and Giannelis (1997); Ren *et al.* (2000)].

Recent work on the creep behavior of intercalated PLS nanocomposite melts indicated that at low strain rates (or shear stresses) the material showed a Newtonian response with very high viscosity [Galgali *et al.* (2001)]. With an increase in shear stress the viscosity dropped by up to two orders of magnitude within a narrow range of stress. Such materials can be considered to exhibit apparent yield-like behavior [Barnes (1999)]. Based on these observations it was suggested that the microstructure of the dispersed clay tactoids undergoes flow-induced orientation above the yield point, which breaks down the network structure and significantly decreases the resistance to flow.

Solomon *et al.* (2001) investigated the transient response of polypropylene nanocomposites in a shear start-up experiment in which a varying rest period was allowed after a large initial pre-shear in the reverse direction. They observed increasing overshoot with the annealing time, indicating microstructural changes during the quiescent period. Further, the transient stress scaled linearly with the clay loading and with the effective strain. It was suggested from these results that clay tactoids form a non-Brownian percolating network that is destroyed by high shear. Stress relaxation after step strain in a polystyrene-*b*-polyisoprene intercalated nanocomposite showed an initial rapid relaxation period that corresponded with the relaxation of the matrix polymer followed by very slow relaxation that seemed to originate from structural reorganization [Ren *et al.* (2000)].

It is apparent from the above discussions that the rheology of PLS nanocomposites is strongly linked to the mesoscopic microstructure of the material. However, rheology by itself is an indirect tool with which to investigate microstructural evolution in complex fluids. Combining rheological characterization with simultaneous structural characterization offers a useful tool with which to directly investigate rheology–microstructure linkages. Several *in situ* techniques such as rheo-optical [Janeschitz-Kreigl (1983)], rheo-x-ray [Sondergaard and Lyngaae-Jorgensen (1995)], rheo-nuclear magnetic resonance (NMR) [Thiele *et al.* (2001), Arola *et al.* (1999)] and rheo-small angle neutron scattering (SANS) [Schmidt *et al.* (2000)] have been used to investigate flow-induced microstructural evolution in structured fluids. Recently, the rheo-SANS technique was used to investigate shear alignment of hectorite clay platelets suspended in an aqueous solution of poly(ethylene oxide) [Schmidt *et al.* (2000)]. It was shown that in Couette geometry the hectorite platelets were oriented in the flow direction with their surface normal to the neutral direction. No correlations with simultaneous rheological measurements were es-

**TABLE I.** Materials used.

| Polymer | $M_w$ | $M_n$ | $M_w/M_n$ |
|---|---|---|---|
| sPP4 | 160 000[a] | 35 555[a] | 4.5[a] |
| sPP10 | 115 000[a] | 31 944[a] | 3.6[a] |
| sPP20 | 87 000[a] | 25 588[a] | 3.4[a] |
| PB3200[c] | 122 700[b] | 44 800[b] | 2.7[b] |

| Clay Grade | CEC of the original montmorillonite | Modifier content | Supplier |
|---|---|---|---|
| C20A | 92 meq/100 g clay | 95 meq/100 g clay | Southern Clay Products, Texas |

[a]Values supplied by the manufacturer.
[b]Obtained by a high temperature-gel permeation chromatography (model PLGPC220 equipped with refractive index (RI) detector and autosampler). The analysis was carried out using 3×mixed B type gel columns with 1,2,3 tricholorobenzene as a mobile phase at 160 °C. The molecular weight and molecular weight distribution reported with respect to polystyrene (PS) std.
[c]Maleic anhydride content: 1 wt %.

tablished in this study. There are no reports so far on coupled rheological and *in situ* structural investigations of deforming PLS nanocomposite melts.

In this article we have used a rheo-x-ray technique to study the flow-induced microstructural evolution in intercalated layered-silicate syndiotactic polypropylene nanocomposites. The paper is organized as follows. Section II describes the materials, apparatus, and experimental techniques used in this work. Section III presents a detailed rheological investigation of the nanocomposites. The purpose of Sec. III is to compile the rheological information obtained from both stress and strain controlled rheometers, which might provide indirect evidence of flow-induced microstructural changes in the nanocomposites. Another purpose of Sec. III is to provide rheological data that can be compared with the direct *in situ* observation of the microstructural evolution described in Sec. IV. The results of rheo-x-ray diffraction (XRD) experiments are summarized in Sec. IV. A discussion of the rheology-microstructure links obtained from the rheology and rheo-x-ray data is given in Sec. V.

## II. EXPERIMENT

### A. Materials

The nanocomposite used are of intercalated type based on a syndiotactic polypropylene matrix and organically modified hydrophobic montmorillonite clays. Three syndiotactic polypropylene resins (Fina Oil and Chemical Co., La Porte, TX, USA) were used as the matrix, the details of which are listed in Table I. Dimethyl dihydrogenated tallow ammonium exchanged montomorillonite clay (C20A) with a modifier concentration of 95 milliequivalent (meq)/100 g was used. The clay was supplied by Southern Clay Products (Gonzales, TX). The clay loadings ranged from 3 to 25 wt %. An isotactic polypropylene-*g*-maleic anhydride copolymer (Polybond 3200, 1 wt % maleic anhydride content, MFI = 140) was used in some cases as a compatibilizer. Two types of nanocomposites were produced, compatibilized and uncompatibilized, depending on whether or not the compatibilizer was added during extrusion (see Table II).

### B. Sample preparation

All nanocomposites were prepared by melt intercalation in a corotating Berstoff ZE-25 twin screw compounder that had screws 25 mm in diameter and $L/D = 41$. Melt compounding was done at 190 °C (the temperature profile of the screw increased from 140 at the feed to 190 °C near the die) and at screw speed of 100 rpm. The compounded melt was water quenched and pelletized. For some rheological measurements the pellets were compression molded into 25 mm diam×1 mm thick disks. Molding was carried out by compressing the pellets at 190 °C followed by slow cooling under pressure.

### C. Rheolgoical measurements

Rheological characterization of the nanocomposites was carried out using three different rheometers, namely, a strain controlled Rheometrics Scientific's RDS-II rheometer, a stress controlled Bohlin CVO-50 rheometer, and the Cambridge MultiPass Rheometer (MPR) [Mackley *et al.* (1995)]. A 25 mm diam parallel plate configuration was used in both the RDS-II and the CVO-50 rheometers, while a 4 mm diam×10 mm length capillary configuration was used in the MPR. All experiments in parallel plate geometry were carried out under a nitrogen blanket to minimize thermo-oxidative degradation. In the MPR, the sample was completely contained between two reciprocating pistons and thus was not exposed to air during the experiment. Experiments performed on the strain-controlled rheometer included dynamic strain sweep, small amplitude oscillatory shear, and stress relaxation after step strain while creep and stress ramp experiments were done using the stress controlled rheometer. The MPR was used to perform steady shear experiments in ''multipass mode'' (which is explained later). No pre-shear was applied before the rheological measurements. Typical waiting periods were 2 and 20 min, respectively, in parallel plate rheometers and MPR before starting the measurements. Care was taken not to subject the samples to strong per-shear before rheological measurements.

### D. Microstructure measurements

XRD was used as the main characterization technique for determining the microstructure of the nanocomposites. The source of the radiation was a Cu $K\alpha$ lab source with 1.5 Å wavelength. Our previous work has shown that transmission electron microscopy gives similar (but more qualitative) results of the microstructure [Galgali *et al.* (2001)]. Hence XRD was used as the principle technique and was found adequate for the purposes of this work. A Rigaku Dmax 2500 diffractometer with a rotating anode generator and a wide angle powder goniometer fitted with a high temperature attachment was used as a preliminary characterization tool for the as-extruded samples. The x-ray generator was operated at 40 kV and 150 mA. Figure 1 shows the diffraction patterns at 190 °C from the organically modified clay, an uncompatibilized hybrid (sPP20/9/0), and a compatibilized hybrid (sPP20/9/9). The presence of a dominant peak indicates that the nanocomposites contain intercalated clay tactoids. The *d* spacing (gallery height) of the clay platelets in the tactoids was about 30 Å in the pure clay, about 32 Å in the uncompatibilized hybrid, and about 34 Å in the compatibilized hybrid. The slight increase in the gallery height for the compatibilized hybrid is an indication of better intercalation, possibly due to the presence of the compatibilizer.

The Cambridge MPR was used for *in situ* rheo-XRD measurements from nanocomposite melts during shearing. Figure 2(a) shows a schematic of the rheo-XRD apparatus. The MPR consists of two pistons, one each located in the top and bottom barrels. The barrel diameter was 15 mm. The reciprocating pistons enclose a fixed volume of the sample and push it backwards and forwards through a center test section like a capillary.

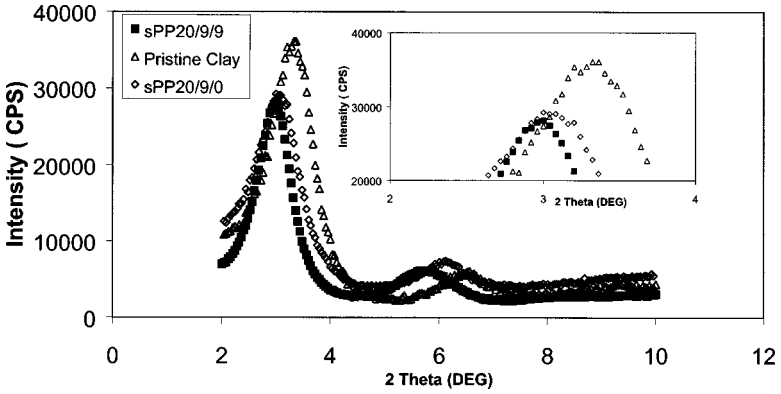


**FIG. 1.** WAXS of clay (C20A), uncompatibilized hybrid (sPP20/9/0), and compatibilized hybrid (sPP20/9/9) using the high temperature Rigaku XRD machine ($T = 190$ °C).

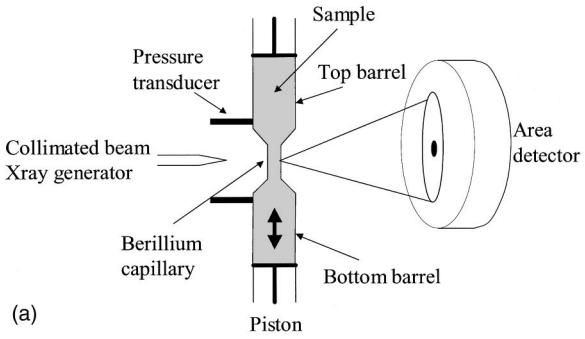


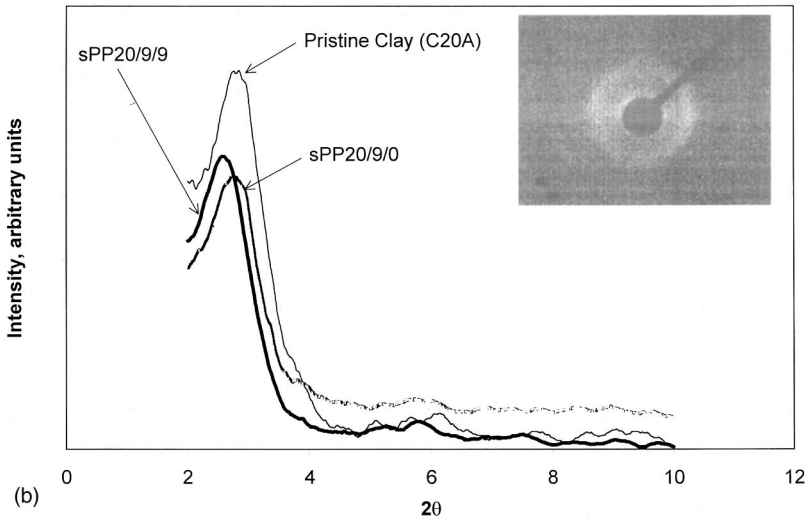


**FIG. 2.** (a) Schematic of the Cambridge MultiPass Rheometer equipped with an *in situ* XRD measurement facility; (b) WAXS of the same samples as those in Fig. 1 but using the MPR rheo-XRD equipment under no-flow conditions at 190 °C. The inset shows the 2D x-ray diffraction pattern of the compatibilized hybrid.

A detailed description of the MPR can be found in the work of Mackley *et al.* (1995) and of Mackley *et al.* (2000). The piston displacements and speeds are precision controlled using a servo hydraulic mechanism. A 4 mm diam×10 mm long capillary made of x-ray transparent beryllium was used as the center section in our experiments. The sample temperature was controlled to within ±0.5 °C by circulating heating oil in the jackets around the barrels and the test section. The piston speeds used in this work ranged from 0.01 to 50 mm/s, which correspond to apparent wall shear rates of 0.28–1406 $s^{-1}$. Experiments were performed at 190 °C. In multipass mode of operation the pistons reciprocated in tandem at a set speed and for a set displacement with rest time between each stroke. Two pressure transducers located near the ends of the capillary measure the drop in pressure across it during each stroke. The uncorrected wall shear stress was calculated from the measured drop in steady state pressure (see Fig. 9) as

$$\tau_w = \frac{\Delta PR}{2L}, \tag{1}$$

where $R$ and $L$ are the radius and length, respectively, of the capillary. The apparent wall shear rate was calculated by the standard relations for Poiseuille flow, namely,

$$\dot{\gamma}_{a,w} = \frac{4Q}{\pi R^3}. \tag{2}$$

Here, $Q = (\pi/4)D_b^2 V_p$ is the flow rate, $D_b$ is the barrel diameter, and $V_p$ is the piston velocity.

The MPR was located in an x-ray diffractometer cabinet such that the capillary was aligned in front of a collimated x-ray beam. The x-ray generator was operated at 45 kV and 45 mA. Various safety interlocks ensured minimum exposure to x rays. Scattered x rays from the sample were collected on an area detector. The distance between the sample and the detector can be varied and thus measurements in both wide and small angle modes can be made. All measurements in this work were made in wide angle mode in the $2\theta$ range of 1°–10°. Thus, the MPR can be used to control the temperature and shear rates while simultaneously allowing *in situ* wide angle x-ray spectroscopy (WAXS) measurements. It is important to note that the sample experiences a nonuniform shear rate in the capillary that varies nonlinearly from zero at the center of the capillary to a maximum at the wall, the value of which depends on the piston speed. Thus, the scattered x-ray signal received by the detector gives an indication of the volume-averaged effects of shear rate (or shear stress) gradients in the sample.

The data collected by the area detector of the MPR-XRD equipment was processed and analyzed to correct for warping, background scattering, smoothing, and peak searching. The peak $2\theta$ positions for pristine C20A clay obtained from the Rigaku Dmax 2500 diffractometer was used as a one-point calibration for converting the diffraction ring data into intensity-$2\theta$ data. Figure 2(b) shows the scattered x-ray intensity from the clay, an uncompatibilized hybrid (sPP20/9/0), and a compatibilized hybrid (sPP20/9/9) under quiescent conditions at 190 °C. The inset in Fig. 2(b) shows, as an example, the two-dimensional diffraction pattern of the compatibilized hybrid. The clay tactoids in the compatibilized nanocomposite have a slightly larger gallery height of 34 Å than that in the uncompatibilized sample or the clay ( ~ 30 Å). These peak positions are similar to those obtained from the Rigaku Dmax 2500 diffractometer (see Fig. 1). The diffraction rings corresponding to the peaks at $2\theta = 6°$ were not easily visible on the area detector. This is because of the lower intensity source of the x rays in the MPR-XRD equipment

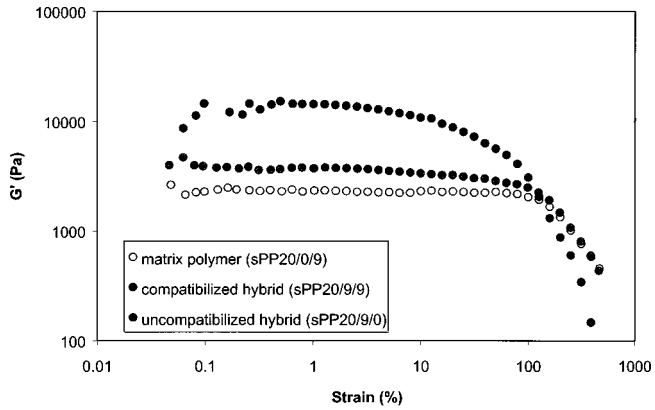


**FIG. 3.** Storage modulus of the matrix polymer (sPP20/0/9), the uncompatibilized hybrid (sPP20/9/0), and the compatibilized hybrid (sPP20/9/9) in a strain sweep experiment at frequency of 10 Hz and $T = 190$ °C.

compared to in the Rigaku machine. Thus, the peak $2\theta$ positions obtained from the Rigaku diffractometer are expected to be more accurate. The MPR-XRD apparatus, on the other hand, was used specifically to obtain data on flow-induced orientation.

Recently, Kaempfer *et al.* (2002) have shown that s-PP nanocomposites prepared by melt intercalation in the presence of an i-PP-*g*-maleic anhydride copolymer as a compatiblizer have a complex microstructure. The compatibilizer is incompatible with the s-PP matrix and forms immiscible domains of the order of 50–100 nm in the blend. In the presence of clay, the i-PP-*g*-maleic anhydride copolymer intercalates within the silicate galleries and encapsulates the clay tactoids to form nanoparticles of core/shell morphology. These nanoparticles are then dispersed into the sPP matrix and form a nanocomposite. Thus, the microstructure of layered silicate s-PP nanocomposites is more complex than that of conventional i-PP based nanocomposites. However, the s-PP nanocomposites show enhancements in mechanical properties that are typical of any well-dispersed intercalated nanocomposites. They also show the characteristics rheological features of intercalated nanocomposites as will be seen later in this article. Thus, for the purpose of the present work we will consider the s-PP nanocomposites as representative examples of the well-dispersed intercalated nanocomposites.

## III. RHEOLOGY

Intercalated PLS nanocomposites are rheologically complex fluids consisting of highly asymmetric colloidal clay tactoids dispersed in a viscoelastic matrix. Several different rheological experiments are required to perform complete characterization of these materials in the linear and nonlinear viscoelastic regimes. In this work we have used a combination of strain controlled and stress controlled rheometers to cover a wide range of the shear rates and shear stresses as well as to study the transient response of the materials.

### A. Linear rheology

A strain sweep dynamic test in which the sample is subjected to increasing oscillatory strain amplitudes at controlled frequency can differentiate the linear and nonlinear regimes. Figure 3 shows the storage modulus obtained from strain sweep tests on three samples, i.e., the matrix polymer (sPP20/0/9), the uncompatibilized hybrid (sPP20/9/0), and compatibilized (sPP20/9/9) hybrid. The transition from the linear to the nonlinear

regime, characterized by the rapid decrease in $G'$, occurs at about 100% strain for the matrix polymer and the uncompatibilized hybrid. For the compatibilized hybrid the transition occurs much earlier, at less than 10% strain, which is similar to the observations of Solomon *et al.* (2001). Further rheological characterizations in the linear regime were done at 2% strain for the compatibilized hybrids, 5% strain for the uncompatibilized hybrid, and 10% strain for the matrix samples.

The results of small amplitude frequency-sweep dynamic experiments on the same three samples are shown in Figs. 4(a)–4(c). The matrix polymer shows classical viscoelastic behavior, namely, a terminal regime at low frequency ($G'' \sim \omega, G' \sim \omega^2$) with $G' < G''$ followed by a crossover at a frequency of 251 $s^{-1}$ after which $G' > G''$. The uncompatibilized hybrid shows a small deviation from classical behavior in that the slopes of $G'$ and $G''$ in the terminal zone are less than 2 and 1, respectively. $G'$ is still less than $G''$ at lower frequencies and a crossover is observed at 200 $s^{-1}$. The behavior of the compatibilized nanocomposite is distinctly different. At low frequency, $G' > G''$ and both $G'$ and $G''$ show distinct nonterminal plateau-like behavior. In the intermediate frequency range, there is a crossover at a frequency of 1.58 $s^{-1}$ into a regime where $G' < G''$. Finally at a frequency of 63 $s^{-1}$, there is a second crossover after which $G' > G''$. The nonterminal behavior of the compatibilized nanocomposite is similar to that reported earlier for other intercalated PLS nanocomposites [Krishnamoorti *et al.* (1996); Krishnamoorti and Giannelis (1997); Ren *et al.* (2000); Galgali *et al.* (2001); Solomon *et al.* (2001)]. The plateau is suggestive of a solid-like response for time scales longer than at least 100 s. The first crossover in the intermediate frequency range is an indication of a transition from the solid-like response to a viscous response. At high frequency, the values of $G'$ for all three samples are similar, indicating that segmental motion of the polymer matrix dictates the material response at short time scales. Thus, the second crossover for the compatibilized sample represents a typical elastic response arising from the matrix polymer.

The apparent solid-like response at long time scales (low frequency) can be better probed by performing creep experiments at small shear stresses. Figure 5 shows the characteristic viscoelastic creep response for all three samples in which the creep compliance rapidly increased at short times (seen clearly in the semilog plot) followed by a slow increase at long times (seen clearly in the inset, which is the same data plotted on linear–linear scale). The creep compliance of the sPP20/9/9 was significantly lower than that of the sPP20/9/0 and sPP20/0/9 samples, which suggested a solid-like response of the compatibilized hybrid. Nonetheless, the compatibilized nanocomposite showed Newtonian behavior at long times; the small but finite slope of $J(t)-$time data at long times indicates large zero-shear viscosity.

### B. Nonlinear rheology

The viscosity at higher stresses (i.e., the nonlinear response) was probed by performing stress ramp experiments, the results of which are shown in Fig. 6(a) for several nanocomposite samples. The matrix polymer showed Newtonian behavior over the whole range of stress, while the uncompatibilized nanocomposites showed slightly higher zero-shear viscosity followed by a small decrease in viscosity at higher stress. The compatibilized samples showed significantly higher zero-shear viscosity followed by a large decrease in viscosity over a narrow range of shear stress. We have independently confirmed that the drop in viscosity is not an artifact of wall slippage. Following the arguments of Barnes (1999) we believe that these data indicate the apparent yield behavior of

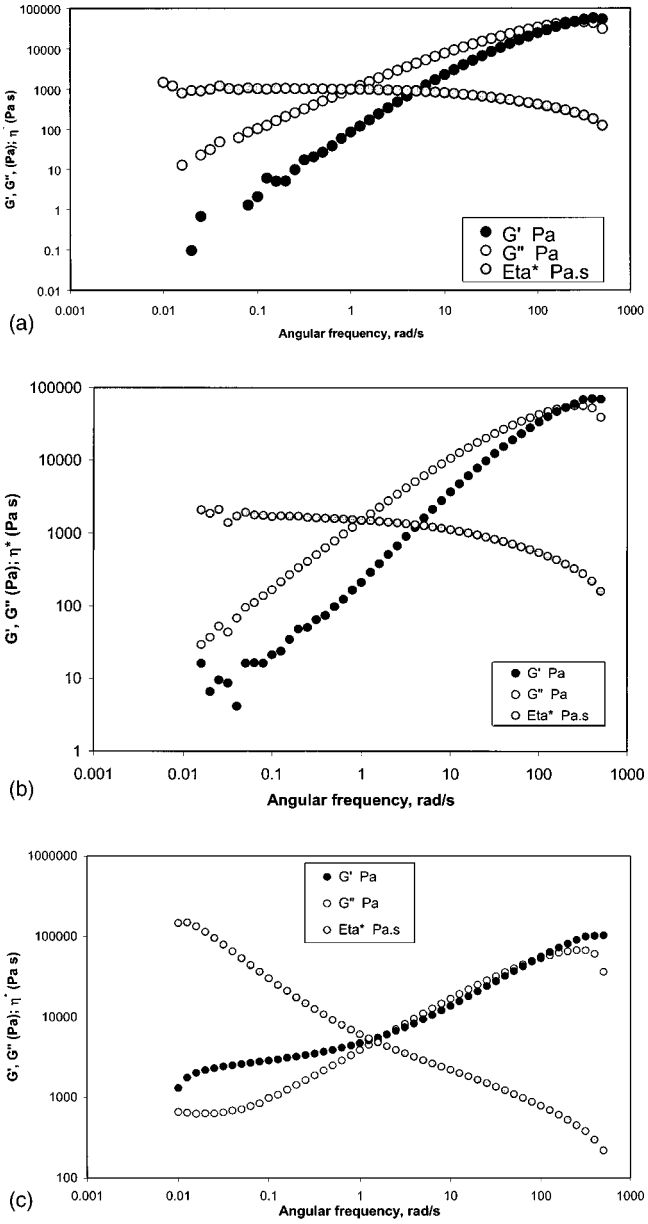


**FIG. 4.** Small amplitude frequency sweep data at 190 °C for (a) the matrix polymer (sPP20/0/9; $\gamma_0 = 10\%$), (b) the uncompatibilized hybrid (sPP20/9/0; $\gamma_0 = 5\%$), and (c) the compatibilized hybrid (sPP20/9/9; $\gamma_0 = 2\%$).

the material above a critical stress level. Yield stress can be arbitrarily defined as the stress at the inflection point in the rapidly decreasing region of viscosity–shear stress data.

A complete picture of the rheological response of sPP20/9/9 over a wide range of shear rates (or stresses) is shown in Fig. 6(b). Data from different rheological experiments, namely, a small amplitude oscillatory shear, stress ramp, and capillary rheometry, are included. At shear rates lower than $10^{-3}$ l/s the nanocomposite behaved like a Newtonian liquid of very high viscosity ( $\sim 2\times10^5$ Pa s). The nonlinear regime began

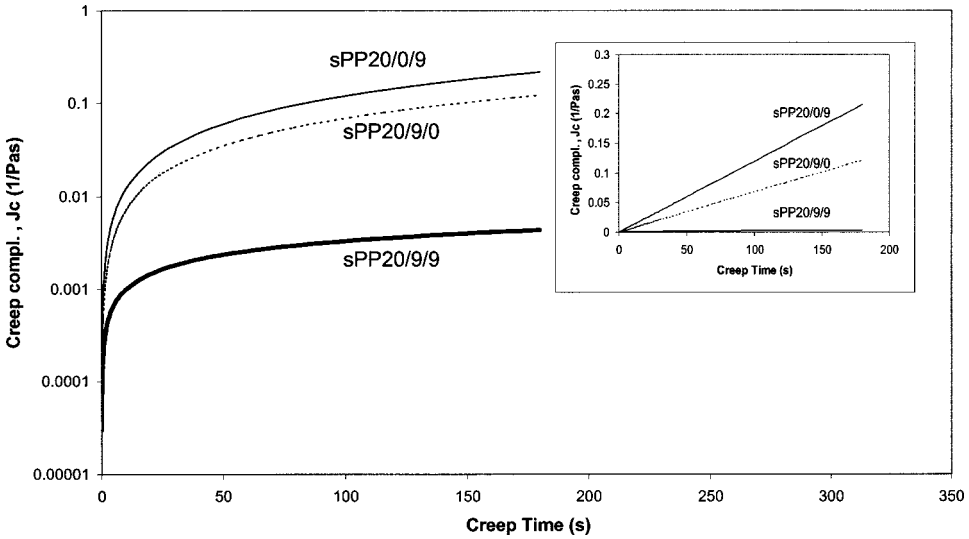


**FIG. 5.** Creep compliance of the matrix polymer, the uncompatibilized hybrid, and the compatibilized hybrid at 190 °C for stress of 10 Pa. The semilog plot shows the short-time response, while the inset shows the long-time response more clearly.

when the material yielded, i.e., deformed significantly for a relatively small increase in stress in the range of approximately $\tau_0 \approx 200-600$ Pa. After the apparent yielding process the shear stress increased again with the shear rate as shown by the MultiPass Rheometer data, which matched well with the stress ramp data obtained from the Bohlin rheometer in the low shear rate range and also with the dynamic data obtained from the RDSII rheometer in the high shear rate range. Interestingly, at low frequency the complex viscosity calculated from the small amplitude data did not match the steady shear data. This implies that the compatibilized nanocomposites did not follow the empirical Cox–Merz rule. Similar observations have been reported by Fornes (2001) and by Krishnamoorti *et al.* (2001). A possible reason for this observation is that the microstructural changes in the material during the two types of tests could be very different and therefore they do not probe the same structure. For instance, the steady shear experiment imposes large strain on the sample, which could result in orientation of the clay tactoids in the nanocomposite and hence a reduction in frictional resistance to flow. Indeed, the sample can yield due to orientation of the microstructure. In the small amplitude oscillatory shear experiment, on the other hand, the microstructure probably does not change significantly due to the small strain and as a result the frictional resistance remains higher. Large amplitude oscillatory shear experiments (not shown here) have indeed shown a decrease in the complex modulus and better matching with the steady shear data. Similar observations have been reported by Ren *et al.* (2000). The steady shear and small amplitude oscillatory shear data matched reasonably well for the uncompatibilized nanocomposites, while the match was almost perfect for the matrix polymers.

## C. Material functions

The rheology of a PLS nanocomposite can be described by three material functions: (a) the zero-shear viscosity $\eta_0$, which provides insight into the microstructure of the

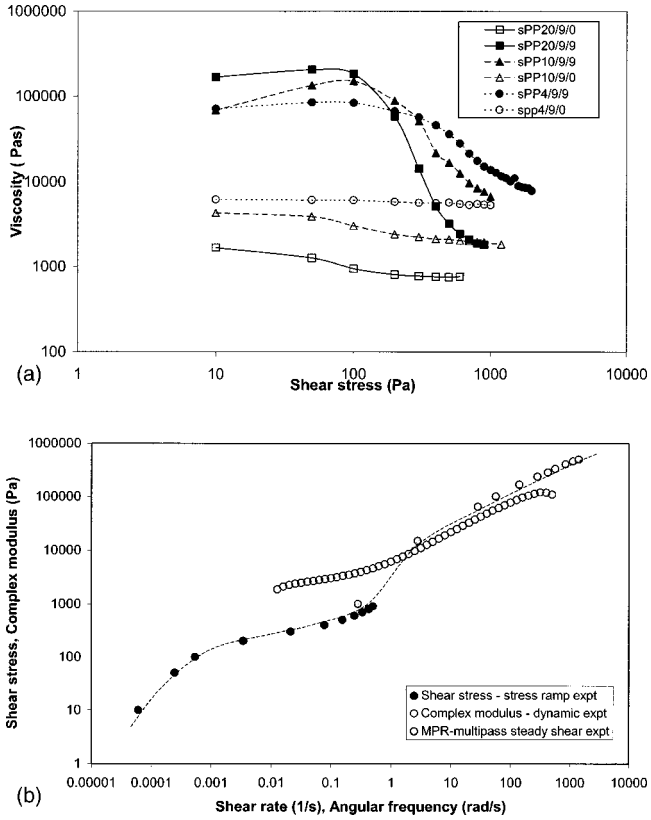


**FIG. 6.** (a) Viscosity of compatibilized and uncompatibilized hybrids made from sPP matrix polymers of various molecular weights. The data were obtained from stress–ramp experiments at 190 °C. (b) Overlay of flow curves obtained from stress–ramp, frequency sweep, and MultiPass experiments for sPP20/9/9; all experiments were done at 190 °C.

material under near-quiescent conditions, (b) the yield stress $\tau_0$, which suggests breakage of the microstructure, and (c) a characteristic relaxation time $\lambda = \eta_0/\tau_0$ of the microstructure.

We have shown earlier that the flow activation energy of iPP nanocomposites (compatibilized and uncompatibilized) obtained from an Arhenius plot of $\ln \eta_0$ vs $1/T$ is no different than that of the matrix polymer [Galgali *et al.* (2001)]. This implies that whereas confinement of the polymer chains within the clay galleries does not contribute to the low shear rheology, it is the frictional resistance of a percolating network of the dispersed clay tactoids that provides the large resistance to flow. Similar ideas were presented by Ren *et al.* (2000) based on the temperature dependence of shift factors observed in linear oscillatory shear experiments.

Figure 7(a) shows plots of $\eta_0$ vs clay loading and $\tau_0$ vs clay loading for compatibilized sPP20 nanocomposites with increasing clay loadings (sPP20/0/0, sPP20/3/3, sPP20/6/6, sPP20/9/9, and sPP20/25/25). The data show that the zero-shear viscosity of the nanocomposites scales exponentially with the silicate loading, which again supports the idea that the microstructure of the nanocomposite consists of a percolating network of well-dispersed clay tactoids at low shear stresses [Bird and Dai (1983)]. On the other hand, the yield stress scales only linearly with silicate loading, which suggests that the yielding process corresponds to destruction of this network.

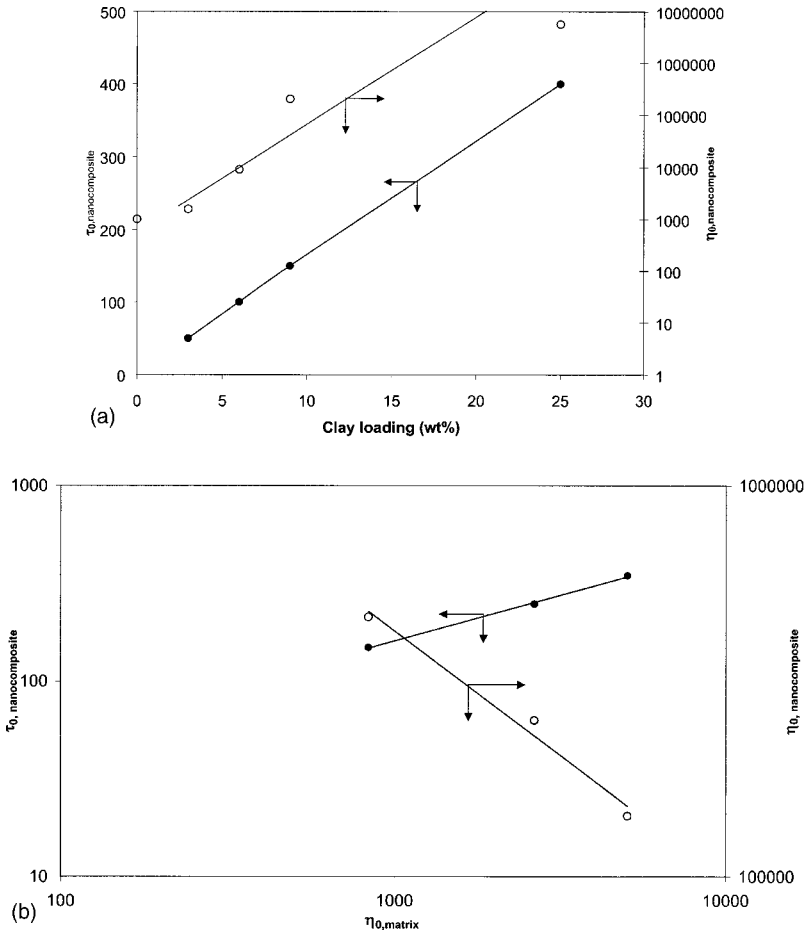


**FIG. 7.** (a) Zero-shear viscosity and yield stress of compatibilized hybrids containing different clay loadings (sPP20/0/0), sPP20/3/3, sPP20/6/6, and sPP20/9/9) at 190 °C as a function of clay loadings. (b) Zero-shear viscosity and yield stress of compatibilized hybrids prepared using matrix polymers of different molecular weights (sPP4/9/9, sPP10/9/9, and sPP20/9/9) at 190 °C as a function of matrix zero-shear viscosity.

Figure 7(b) shows the plots of $\eta_{0,\text{nanocompsoite}}$ vs $\eta_{0,\text{matrix}}$ and $\tau_{0,\text{nanocomposite}}$ vs $\eta_{0,\text{matrix}}$ for compatibilized sPP nanocomposites of same clay loading but of different molecular weight sPP resins (sPP4/9/9, sPP10/9/9, and sPP20/9/9). This plot shows an interesting observation in that as the zero-shear viscosity of the matrix decreases, the zero-shear viscosity of the corresponding nanocomposites increases. This suggests that the zero-shear viscosity of the nanocomposites is determined largely by the microstructure of the percolating network of clay tactoids but not by the zero-shear viscosity of the resin. It is possible that the smaller chains of a matrix having lower viscosity would intercalate the clay tactoids to a greater extent thereby leading to better dispersion and hence to a higher $\eta_0$ value. On the other hand, the yield stress of the nanocomposite increases with the zero-shear viscosity of the matrix resin. This suggests that, once the network is destroyed during yielding, the yield stress is dictated by the matrix properties rather than by the microstructure of the clay.

The characteristic relaxation time for the microstructure in sPP20/9/9 nanocomposite can be estimated as $\lambda = \eta_0/\tau_0 \sim 2\times10^5/200 = 10^3$ s. This agrees with the inverse of

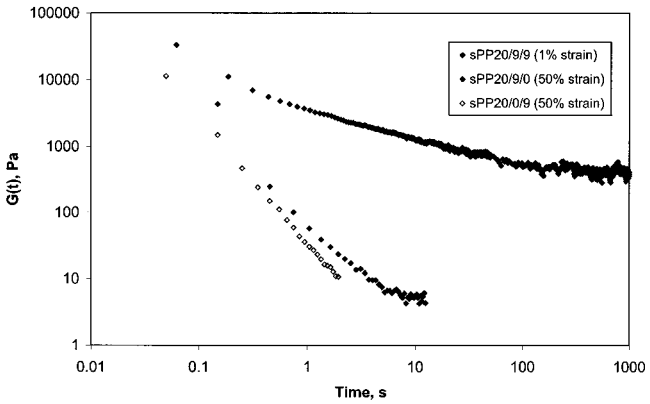


**FIG. 8.** Stress relaxation after step strain for the matrix polymer (sPP20/0/9; 50% step strain), uncompatibilized hybrid (sPP20/9/0; 50% step strain), and compatibilized hybrid (sPP20/9/9; 1% step strain).

the shear rate at which yielding begins [Fig. 6(b)] and suggests that below this shear rate the microstructure has sufficient time to relax and maintain the percolating network, while above this shear rate the network breaks down.

### D. Transient experiments

Stress relaxation experiments provide information about the microstructural relaxation mechanisms and time scales in the linear and nonlinear viscoelastic regimes [Osaki (1993)]. Figure 8 shows the stress relaxation of three samples after step strain in the linear regime. Based on the strain sweep data (Fig. 3) step strain of 50% was used for the matrix polymer (sPP20/0/9) and for the uncompatibilized nanocomposite (sPP20/9/0), while step strain of 1% was used for the compatibilized nanocomposite (sPP20/9/9). Apart from the slightly higher relaxation modulus of the uncompatibilized sample, its stress relaxation behavior was qualitatively similar to that of the matrix polymer. Data for time longer than 1 s for the matrix and the uncompatibilized hybrids are noisy and therefore are not reported here. For the compatibilized hybrid the relaxation modulus at very short times ( $< 0.2$ s) was similar to that of the uncompatibilized and the matrix polymers. The stress level at very short times (0.06 s) can be calculated to be approximately 300 Pa. Thus, upon sudden step strain deformation the material was subjected to a stress level that is near the yield point. It can be seen that the stress relaxed very slowly after the initial rapid relaxation and reached a plateau at very long times of $\sim 10^3$ s, which corresponds with the characteristic microstructural relaxation time estimated earlier.

The different rheological experiments described above give consistent and complementary information about the flow behavior of layered-silicate syndiotactic polypropylene nanocomposites. First, the rheological data show that, although the *d* spacings in the compatibilized and the uncompatibilized hybrids indicated by WAXS are not significantly different, their rheological behavior is vastly different. This suggests that the principle difference in the microstructure of these materials is the state of dispersion of the clay tactoids in the matrix. The clay is expected to be well dispersed in the compatibilized hybrids. Second, the rheological data indirectly suggest that the complex viscoelastic behavior is linked with deformation-induced microstructural changes in the materials. Direct evidence of microstructural changes would be desirable to confirm rheological

**TABLE II.** Samples used for rheological and rheo-XRD experiments.

| Sample code | Matrix polymer | Clay loading (wt %) | Compatiblizer (wt %) | Experiment |
|---|---|---|---|---|
| Nanocomposites containing different clay loadings | | | | |
| sPP20/3/3 | sPP, MFI-20 | 3 | 3 | Rheology |
| sPP20/6/6 | sPP, MFI-20 | 6 | 6 | Rheology |
| sPP20/9/9 | sPP, MFI-20 | 9 | 9 | Rheology |
| sPP20/25/25 | sPP, MFI-20 | 25 | 25 | Rheology |
| Matrix resins of different molecular weights | | | | |
| sPP20/0/9 | sPP, MFI-20 | 0 | 9 | Rheology |
| sPP10/0/9 | sPP, MFI-10 | 0 | 9 | Rheology |
| sPP4/6/6 | sPP, MFI-4 | 0 | 9 | Rheology |
| Nanocomposites with matrix resins of different molecular weights | | | | |
| sPP20/9/9 | sPP, MFI-20 | 9 | 9 | Rheology and rheo-XRD |
| sPP20/9/0 | sPP, MFI-20 | 9 | 0 | Rheology and rheo-XRD |
| sPP10/9/9 | sPP, MFI-10 | 9 | 9 | Rheology |
| sPP10/9/0 | sPP, MFI-10 | 9 | 0 | Rheology |
| sPP4/9/9 | sPP, MFI-4 | 9 | 9 | Rheology and rheo-XRD |
| sPP4/9/0 | sPP, MFI-4 | 9 | 0 | Rheology and rheo-XRD |

understanding. In Sec. IV we investigate some crucial rheology-microstructure links by using the *in situ* rheo-XRD technique.

## IV. RHEO-XRD

Two types of experiments were performed in the rheo-XRD MPR apparatus (see Table II). In the first experiment the samples were subjected to steady shear in multipass mode in which the pistons were reciprocated at a set velocity with a short rest time of 1 s between each of the strokes. The piston movement and the corresponding difference in pressure data during one cycle of a typical test for a representative sample (sPP20/9/9) are shown in Fig. 9. When the pistons start moving the difference in pressure rapidly

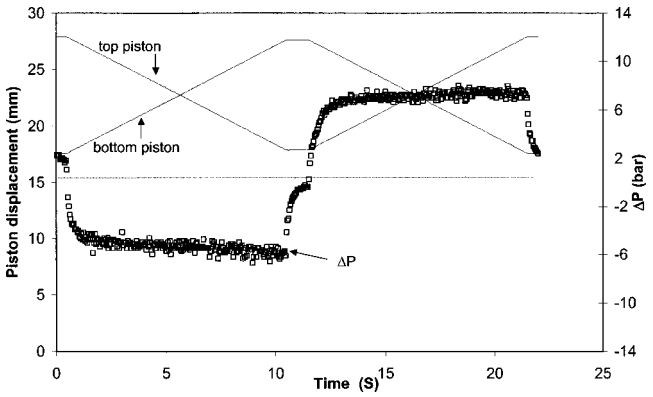


**FIG. 9.** Typical rheological data from a MultiPass experiment: $V_p = 1$ mm/s, maximum piston displacement = 10 mm.

increases and reaches a steady state value. The wall shear stress can then be calculated from Eq. (1). When the pistons stop the pressure difference decreases rapidly but before it can relax completely the next cycle begins after the short rest time. The wall shear stress calculated from the measured difference in pressure according to Eq. (1) at different piston speeds was plotted earlier in Fig. 6(b).

The XRD data were collected simultaneously during these multipass runs. The data collection time was set to 4 min to allow sufficient signal intensity. The diffraction patterns for the compatibilized hybrid sPP20/9/9 at different piston velocities are shown in Fig. 10(a) and the corresponding integrated intensity along the azimuthal direction (for $1 < 2\theta < 10°$) is plotted alongside. When the pistons were at rest, the diffraction pattern was an almost uniform ring [Fig. 2(b)], which corresponds to the Bragg diffraction by the clay platelets that stack up to form the clay tactoids. At the smallest achievable piston speed of 0.01 mm/s in the MPR (corresponding to an apparent wall shear rate of $\dot{\gamma}_a = 0.28\ \text{s}^{-1}$) there is already an increase in scattered intensity near the equator of the ring. With an increase in piston speed the full diffraction ring disappears and a distinct equatorial band of high intensity is seen. The integrated intensity patterns show two corresponding sharp peaks at the azimuthal angles of $\chi = 90°$ and 270° (where $\chi = 0°$ at the 12 o'clock position in the diffraction pattern). Above 10 mm/s piston speed ($\dot{\gamma}_a = 280\ \text{s}^{-1}$) the equatorial diffraction pattern remains almost unchanged. The appearance of the equatorial diffraction pattern is a clear indication of shear-induced alignment of the clay tactoids along the flow direction with their faces normal to the gradient and x-ray beam direction as shown schematically in Fig. 10(a). Further, the appearance of a band rather than spots suggests the presence of a hierarchy of long-range order that might possibly have been formed due to exfoliation of a few platelets from the edges of the tactoids or due to stacking of oriented clay tactoids. At comparable piston speeds the uncompatibilized hybrid was oriented to a smaller extent than the compatibilized hybrid as shown in Fig. 10(b) for a piston speed of 10 mm/s. Also, the absence of a distinct equatorial band is notable and instead an equatorial alignment along the diffraction ring was seen. This is clearly seen as a flat peak in the intensity–$2\theta$ plot for the compatibilized sample and a sharp peak for the uncompatibilized sample in Fig. 10(b).

The degree of orientation can be quantified by an average orientation function defined as [Ugaz and Burghardt (1998)]

$$S = \frac{-2\int_0^{\pi/2} I(\chi)P(\chi)\sin\chi d\chi}{\int_0^{\pi/2} I(\chi)\sin\chi d\chi}. \tag{3}$$

Here $I(\chi)$ is the intensity at the azimuthal angle $\chi$ and $P(\chi) = (3\cos^2\chi - 1/2)$ is the Herman orientation function. The orientation function takes values of $S = 0$ and 1 for random orientation and perfect uniaxial orientation, respectively. Figure 11 shows the orientation function plotted against the wall shear stress that is calculated from the measured drop in pressure at each piston velocity. The orientation increased with shear stress and reached a saturation value of approximately 0.85. An orientation function of 0.85 is slightly higher than that obtained in typical thermotropic liquid crystalline polymer melts under high shear [Gervat *et al.* (1995); Ugaz *et al.* (2001)]. However, it is less than that seen in uniaxially oriented fibers.

In Fig. 11 we also show the viscosity–shear stress data for the same sample obtained from the stress ramp experiment in the controlled stress rheometer and the steady shear experiments in the MPR. The data in Fig. 11 clearly show that large scale orientation of the clay tactoids occurred after yielding in a low viscosity matrix. Extrapolation of the orientation data to low stresses suggests that a small amount of orientation that is perhaps

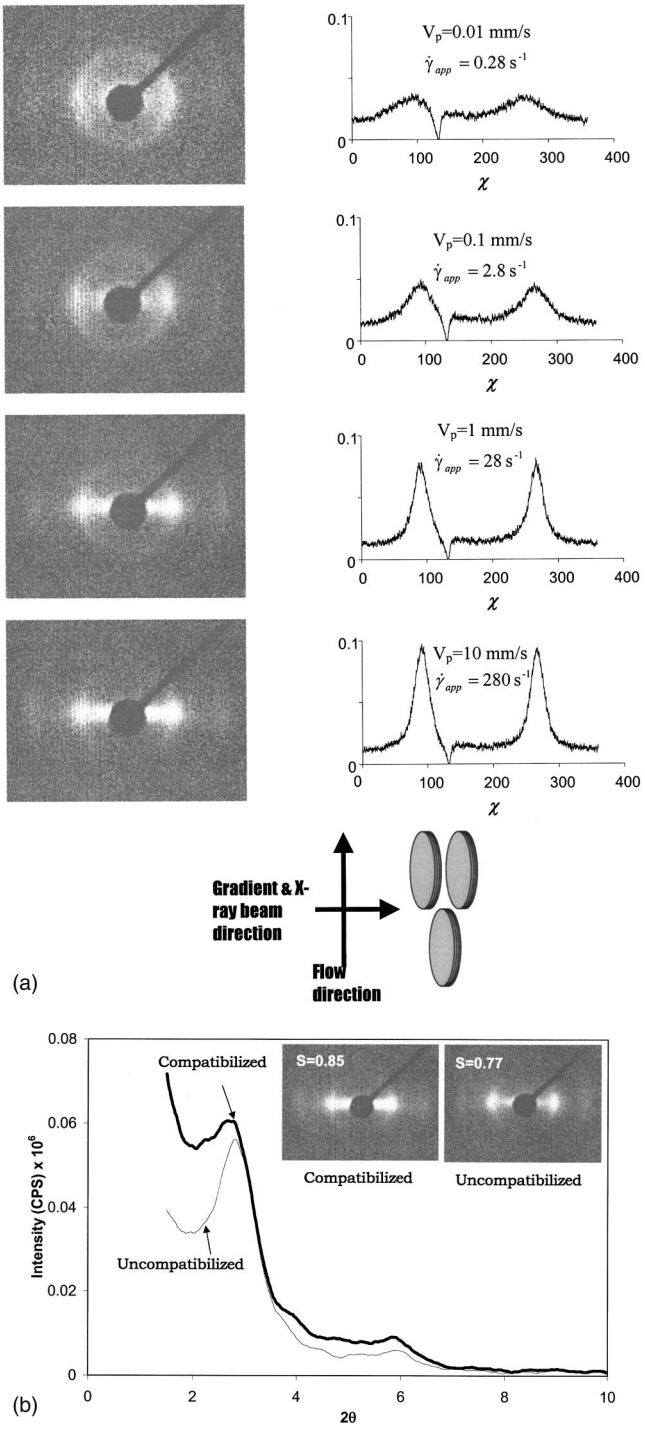


**FIG. 10.** (a) Diffraction patterns of the compatibilized hybrid (sPP20/9/9) at different piston velocities and schematic of the inferred orientation of the clay tactoids. (b) Comparison between the diffraction patterns of compatibilized and uncompatibilized hybrids at a piston velocity of $V_p = 10$ mm/s.

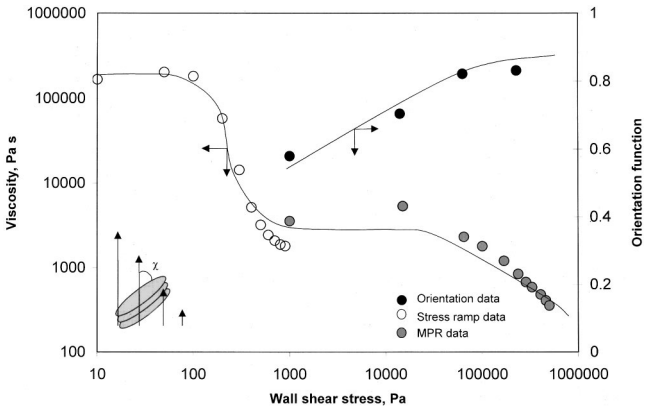


**FIG. 11.** Orientation function and viscosity of the compatibilized hybrid (sPP20/9/9) as a function of wall shear stress at 190 °C.

just sufficient to break the percolating network is responsible for the yield transition. It should be noted that in the rheo-XRD experiment only a small volume of the sample near the capillary wall experiences the shear stress plotted in Fig. 11. The remainder of the sample experiences linearly decreasing stress down to zero at the center. Accordingly, the orientation function could be plotted against a volume average stress, $\bar{\sigma} = 2\sigma_{w/3}$, however, this does not distinctly change the results shown in the Fig. 11. This appears to be the first time that a link between shear rheology and flow-induced orientation has been demonstrated in intercalated PLS-nanocomposite melts using an *in situ* technique. A recent paper has described elongation flow-induced orientation of clay particles in polypropylene nanocomposites using *ex situ* transmission electron microscopy (TEM) [Okamoto *et al.* (2001)].

In the second type of rheo-XRD experiment the relaxation of orientation after cessation of shear was investigated for the uncompatibilized (sPP20/9/0) and compatibilized (sPP20/9/9) nanocomposites. Orientation relaxation of individual colloidal particles under quiescent conditions is expected to occur by Brownian motion, which can be described by the simple equation [Alexander and Johnson (1949)],

$$\frac{\partial f}{\partial t} = \Theta \frac{\partial^2 f}{\partial \phi^2}, \tag{4}$$

where $f(\phi,t)$ is the fraction of particles oriented at angle $\phi$ at time $t$ and $\Theta$ is the rotational diffusion coefficient. The orientation relaxation can be expected to follow an exponential decay function starting from an initial condition $f_0$ corresponding to the pre-shear orientation. Thus,

$$f \approx f_0 e^{-t\Theta}. \tag{5}$$

For an ellipsoidal particle the rotational diffusivity is related to the particle dimensions and to the matrix viscosity [Alexander and Johnson (1949)] by

$$\Theta = \frac{3kT}{16\pi \eta_{\text{matrix}} a^3}\left[2\ln\left(\frac{2a}{b}\right) - 1\right]. \tag{6}$$

Here, $a$ and $b$ are the dimensions of an ellipsoidal particle along the major and minor axes, $\eta_{\text{matrix}}$ is the matrix viscosity, $k$ is the Boltzmann constant, and $T$ is the absolute

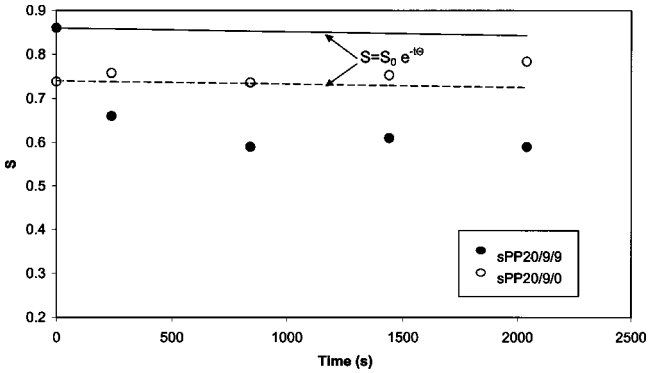


**FIG. 12.** Relaxation of orientation after the cessation of steady shear ($V_p = 1$ mm/s, $T = 190\,°C$). Closed circles represent data for the compatibilized hybrid (sPP20/9/9) and open circles represent data for the uncompatibilized hybrid (sPP20/9/0).

temperature. The physical dimensions of the montmorillonite used in the present work is expected to be similar to that used by Ren *et al.* (2000)] so the clay tactoids can be approximated as disk-like particles having approximate dimensions of $a = 500$ nm (diameter) and $b = 30$ nm (thickness) [Ren *et al.* (2000)]. The sPP20 matrix has zero-shear viscosity of about 833 Pa s at 190 °C. Substituting these values into Eq. (6) gives a rotation diffusivity of $\Theta \sim 10^{-6}$ l/s. Thus, individual, noninteracting clay tactoids can be expected to relax very slowly due to the high aspect ratio and the high viscosity of the polymer melt matrix.

The orientation relaxation experiments were conducted by pre-shearing the samples for about 10 min in multipass mode and then stopping piston motion suddenly while continuing to record the scattered intensity at regular intervals after the cessation of shear. Data were collected for 4 min each 0, 10, 20, and 30 min after the cessation of shear. Due to the finite compressibility of the polymer melt, it continues to flow in the capillary for a short time, approximately 10 s, immediately after stopping the piston motion [Ranganathan *et al.* (1999)]. However, this time is small compared to the XRD data collection time of 4 min so the first data point can be assumed to be a true representation of the initial orientation relaxation after the cessation of shear. The orientation function was calculated from Eq. (3). Figure 12 shows the relaxation of orientation for the compatibilized (sPP20/9/9) and uncompatibilized (sPP20/9/0) samples that were pre-sheared at 1 mm/s piston speed. The lines show the theoretically expected decay of orientation of individual tactoids as per Eq. (5); the dashed line is for the uncompatibilized hybrid and the full line is for the compatibilized hybrid. The initial orientation of the uncompatibilized hybrid is lower than that of the compatibilized hybrid and also relaxes very slowly, in agreement with the theoretical prediction at least during the experiment time scale explored here. In contrast, the initial orientation of the compatibilized hybrid relaxes more rapidly over the first $10^3$ s compared to the theoretical prediction. After this time, the orientation remains constant at about $S = 0.65$. Experimental data for nanocomposites of lower clay loading of approximately 7 wt % also showed a similar trend of rapid initial relaxation followed by slower relaxation to a value of about $S = 0.4$. Experiments at very low clay loading (such as 3 wt %) were not possible due to the reduced scattering intensity. It appears therefore that the rapid initial relaxation is caused by factors other than simple Brownian motion. One possible reason could be the attractive forces between clay tactoids that act like a body force for relaxation. However, the much slower relax-

ation of the clay tactoids in the uncompatibilized hybrids of similar clay loading suggests that attractive forces may not be the cause of the rapid relaxation. It is possible that if the polymer chains of the matrix are coupled with the clay platelets then the stress relaxation of the matrix polymer might accelerate the orientation relaxation of the clay tactoids. The expected absence of such coupling in the uncompatibilized hybrid could explain the much slower relaxation as well as the smaller orientation of the clay in this sample.

## V. SUMMARY OF RHEOLOGY-MICROSTRUCTURE LINKS

The rheology of compatibilized intercalated PLS-nanocomposite melts indicates that at low strain and shear rates (or low stresses) the microstructure of the material consists of a percolating three-dimensional network of dispersed clay tactoids. In this state the melt has a high Newtonian zero-shear viscosity. At high stresses (or shear rates) this network breaks and the material shows yield behavior. Rheology indirectly indicates that yielding might be linked to the orientation of the clay tactoids. The characteristic microstructural relaxation time was estimated to be about $10^3$ s from the stress ramp and the stress relaxation data.

The rheo-XRD experiments at different shear rates provide the first direct evidence of flow-induced orientation of clay tactoids in PLS nanocomposite melts. A high degree of orientation was observed at shear stresses greater than the yield stress. Extrapolation of the orientation data to low stresses suggests that yielding is associated with a small amount of orientation that is perhaps just enough to break the percolating network structure. The rheological data for the uncompatibilized hybrid showed much smaller zero-shear viscosity and much less pronounced yield-like behavior. The corresponding rheo-XRD data showed small orientation of the clay.

Another rheology-microstructure link is obtained from the transient experiments. The orientation relaxation experiments after the cessation of shear showed that the clay tactoids relax their orientation incompletely in approximately 1000 s after which the orientation remains frozen in. Correspondingly, the stress relaxation data show relaxation in 1000 s followed by a plateau in the modulus. The orientation relaxation time scale from the rheo-XRD measurements matched the characteristic microstructural relaxation time scale estimated from the rheological data. Since the Brownian relaxation time scale is expected to be much longer, it is possible that the stress relaxation of the matrix chains, which are compatibilized with the clay platelets, drives the orientation relaxation in about $10^3$ s. After this time scale the clay tactoids are jammed and produce a percolating network that has a residual orientation and a residual relaxation modulus. In the case of a steady shear experiment, at shear rates of below $10^{-3}$ $s^{-1}$ the clay tactoids would have sufficient time to relax their orientation and the hence give a response corresponding to that of a percolating network. At shear rates above $10^{-3}$ $s^{-1}$ the clay tactoids will have insufficient time to relax their orientation, which will trigger destruction of the network and cause a yield-like response. The stress relaxation data for the uncompatibilized hybrid indicate that relation of matrix polymer is decoupled from that of the weak structure formed by the clay. Thus, most of the stress in a step–strain experiment is borne by the polymer matrix, which then relaxes in a manner similar to that of the pure polymer melt. The corresponding rheo-XRD data also suggest that the orientation is smaller during pre-shear and relaxes extremely slowly and independently of the matrix polymer.

## ACKNOWLEDGMENTS

The authors acknowledge the generous gift of montmorillonite clay from Southern Clay Products and of syndiotactic polypropylene from Total Fina. They acknowledge the

help of Deepa Dhoble for high temperature GPC measurements. One of the authors (A.L.) is grateful to the EPSRC, UK, and a second author (G.G.) to the CSIR, India, for financial assistance.

## References

Alexander, A. E. and P. Johnson, *Colloid Science* (Oxford University Press, Oxford, 1949).

Arola, D. F., R. L. Powell, G. A. Barrall, and M. J. McCarthy, ''Point-wise observations for rheological characterization using nuclear magnetic resonance imaging,'' J. Rheol. **43**, 9–30 (1999).

Barnes, H. A., ''The yield stress—A review or $\pi\alpha\nu\tau\alpha\rho\varepsilon\vartheta$—everything flows?'' J. Non-Newtonian Fluid Mech. **81**, 133–178 (1999).

Bird, R. B. and G. C. Dai, ''The rheology and flow of viscoplastic materials,'' Rev. Chem. Eng. **1**, 2–72 (1983).

Brunside, S. D. and E. P. Giannelis, ''Syntehsis and properties of new poly(dimethysiloxane) nanocomposites,'' Chem. Mater. **7**, 1597–1600 (1995).

Fornes, T. D., P. J. Yoon, H. Keskkula, and D. R. Paul, ''Nylon 6 nanocomposites: The effect of matrix molecular weight,'' Polymer **42**, 9929–9940 (2001).

Galgali, G., C. Ramesh, and A. K. Lele, ''A rheological study on the kinetics of hybrid formation in polypropylene nanocomposites,'' Macromolecules **34**, 852–858 (2001).

Gervat, L., M. R. Mackley, T. M. Nicholson, and A. H. Windle, ''The effect of shear on thermotropic liquid crystalline polymers,'' Philos. Trans. R. Soc. London, Ser. A **350**, 1–27 (1995).

Janeschitz-Kreig, H., *Polymer Melt Rheology and Flow Birefringence* (Springer, Berlin, 1983).

Kaempfer, D., R. Thomann, and R. Mulhaupt, ''Melt compounding of syndiotactic polypropylene nanocomposites containing organophilic layered silicates and in-situ formed core/shell nanoparticles,'' Polymer **43**, 2909–2916 (2002).

Kim, G. M., D. H. Lee, and B. Hoffmann, ''Infleunce of nanofillers on the deformation process in layered silicate/polyamide-12 nanocomposites,'' Polymer **42**, 1095–1100 (2001).

Kojima, M., A. Usuki, A. Okada, and O. Kamigato, ''Mechanical properties of nylon6-clay hybrids,'' J. Mater. Res. **8**, 1185–1189 (1993).

Krishnamoorti, R. and E. P. Giannelis, ''Rheology of end-tethered polymer layered silicate nanocomposites,'' Macromolecules **30**, 4097–4102 (1997).

Krishnamoorti, R., R. A. Vaia, and E. P. Giannelis, ''Structure and dynamics of polymer layered silicate nanocomposites,'' Chem. Mater. **8**, 1728–1734 (1996).

Krishnamoorti, R., J. Ren, and A. Silva, ''Shear response of layered silicate nanocomposites,'' J. Chem. Phys. **114**, 4968–4973 (2001).

Mackley, M. R., G. D. Moggridge, and O. Saquet, ''Direct experimental evidence for flow-induced fibrous polymer crystallization occurring at a solid-melt interface,'' J. Mater. Sci. **35**, 5247–5253 (2000).

Mackley, M. R., R. T. J. Marshall, and J. B. A. F. Smeulders, ''The multipass rheometer,'' J. Rheol. **39**, 1293–1309 (1995).

Messersmith, P. B. and E. P. Giannelis, ''Synthesis and characterization of layered silicate-epoxy nanocomposites,'' Chem. Mater. **6**, 1719–1725 (1994).

Okamoto, M., P. H. Nam, P. Maiti, T. Kotaka, N. Hasegawa, and A. Usuki, ''A house of cards structure in polypropylene/clay nanocomposites under elongational flow,'' Nanoletters **1**, 295–298 (2001).

Osaki, K., ''On the damping function of shear relaxation modulus for entangled polymers,'' Rheol. Acta **32**, 429–437 (1993).

Ranganathan, M., M. R. Mackley, and P. J. H. Spiteller, ''The application of a multipass rheometer to time-dependent capillary flow measurements of a polyethylene melt,'' J. Rheol. **43**, 443–451 (1999).

Ren, J., A. S. Silva, and R. Krishnamoorti, ''Linear viscoelasticity of disordered polystyrene-polyisoprene block copolymer based layered-silicate nanocomposites,'' Macromolecules **33**, 3739–3746 (2000).

Schmidt, G., A. I. Nakatani, P. D. Butler, A. Karim, and C. C. Han, ''Shear orientation of viscoelastic polymer-clay solutions probed by flow birefringence and SANS,'' Macromolecules **33**, 7219–7222 (2000).

Solomon, M. J., A. S. Almusallam, K. F. Seefeldt, A. Somwangthanaroj, and P. Varadan, ''Rheology of polypropylene/clay hybrid materials,'' Macromolecules **34**, 1864–1872 (2001).

Sondergaard, K. and J. Lyngaae-Jorgensen, *Rheo-Physics of Multiphase Polymer Systems* (Technomic, Basel, 1995).

Thiele, T., J.-F. Berret, S. Müller, and C. Schmidt, ''Rheology and nuclear magnetic resonance measurements under shear of sodium dodecyl sulfate/decanol/water nematics,'' J. Rheol. **45**, 29–48 (2001).

Ugaz, V. M., W. R. Burghardt, W. Zhou, and J. A. Kornfield, ''Transient molecular orientation and rheology in flow aligning thermotropic liquid crystalline polymers,'' J. Rheol. **45**, 1029–1063 (2001).

Ugaz, V. M. and W. R. Burghardt, ''In-situ x-ray scattering study of a model thermotropic copolyester under shear: Evidence and consequences of flow-aligning behaviour,'' Macromolecules **31**, 8474–8484 (1998).